Journal of Theoretical and Applied Mechanics, Sofia, Vol.55 (2025) pp. 289-301
INTERDISCIPLINARY TOPICS

NUMERICAL STUDY OF PRESSURE FIELD UNDER VARIOUS REGIME FLOW INSIDE RECESS OF AN ORIFICE COMPENSATED HYDROSTATIC BEARING

SLIMANE GHOUAS[1], FAIZA GHEZALI[2*], AHMED BOUZIDANE[3], TAYEB YAHIAOUI[1], THOMAS MARC[4]

[1]*Laboratory of Aeronautics and Propulsion Systems, Faculty of Mechanics, University of Science and Technology of Oran - Mohammed Boudiaf, B.O. Box 1505, El-M'Naouer, 31000, Oran, Algeria*
[2]*Structural and Solid Mechanics Laboratory, Department of Mechanical Engineering, Djillali Liabes's University of Sidi Bel Abbès, BP 89 BEN mhidi, Sidi-Bel-Abbès (22000), Algeria*
[3]*Research Laboratory of Industrial Technologies, Department of Mechanical Engineering, University Tiaret, BP 78 City/Province, Tiaret 14000, Algeria*
[4]*Department of Mechanical Engineering, École de Technologie Supérieure, 1100 Notre-Dame Street West, Montreal, Quebec, (H3C 1K3), Canada*

[Received: 6 February 2025. Accepted: 15 June 2025]

doi: https://doi.org/10.55787/jtams.25.55.3.289

ABSTRACT: This research investigates the effects of regime flow in recess on the pressure distribution within a hydrostatic bearing flat pad supplied by an orifice restrictor. The validation of the findings is conducted using Reynolds' analytical method, which demonstrates a strong correlation with computational fluid dynamics (CFD) simulations, particularly when the Reynolds number in the recess is maintained below 1000. The simulations were carried out using the SST-kω turbulence model. The results reveal that a reduction in viscosity has a pronounced effect on lubrication efficiency. Furthermore, it was observed that deeper recesses yield a more uniform pressure distribution in contrast to shallower recesses, and an increase in the eccentricity ratio results in the presence of the Rayleigh step throughout the entire pressure supply spectrum.

KEY WORDS: hydrostatic bearing, SST k-ω, Rayleigh step, inertia effect, lubricant.

1 INTRODUCTION

In recent years, there has been significant scholarly interest in hydrostatic and hybrid journal bearings, attributed to their extensive applications in engineering fields such as high-speed turbomachinery, machine tool spindles, cryogenic systems, and precision grinding spindles [1–4]. Nevertheless, despite this focus, it remains crucial to enhance our understanding of the flow regimes—whether laminar or turbulent—and the corresponding pressure patterns within the recess flow phenomena to accu-

*Corresponding author e-mail: faiza.ghezali@univ-sba.dz

rately assess the performance characteristics of hydrostatic and hybrid journal bearings. Numerous comprehensive research studies have been published that explore the impact of hydrostatic pocket geometry on flow patterns and pressure distribution, employing both dimensionless formulations of the two-dimensional Navier-Stokes equations [5–9] and three-dimensional Navier-Stokes equations [10–12]. This study aims to elucidate the effects of regime flow in recess on the pressure distribution within a hydrostatic bearing flat pad, which is supplied by an orifice restrictor and influenced by orifice inertia. The pressure distribution and comprehensive flow characteristics of the bearing are determined by solving the full 3D Navier-Stokes equations utilizing the SST k-ω model. The finite volume method, as implemented in ANSYS-CFX software, is employed for this purpose. This research examines the impact of various factors including the pressure flow Reynolds number, recess depths, viscosity, and static eccentric ratio on the pressure profile. The findings are thoroughly discussed, analyzed, and compared with a Reynolds equation approach, which is limited to laminar flow conditions in the recess of a hydrostatic bearing. The results indicate a strong correlation between the computational fluid dynamics (CFD) and Reynolds equation methodologies when the Reynolds number in the recess is below 1000.

2 Research Objective

The objective of this study is to elucidate the impact of regime flows during recess on the pressure distribution within a hydrostatic bearing flat pad supplied by an orifice restrictor and influenced by orifice inertia. This research employs numerical simulations conducted through ANSYS-CFX software. The pressure distribution and comprehensive flow characteristics of the bearing are determined by solving the full 3D Navier-Stokes equations utilizing the SST k-ω model. The finite volume method, as integrated within the ANSYS-CFX software, is applied.

3 Research Materials and Methods

3.1 Hydrostatic bearing description

Figure 1 illustrates a cross section of a rectangular hydrostatic bearing. This bearing is supplied with external pressure (supply pressure P_s) via an orifice restrictor, directing fluid into the recess volume, which subsequently flows into the film lands through the edge discontinuity of the recess. It is important to note that the fluid entering through the orifice is presumed to have a uniform velocity, and the exit velocity fields are identical across the side film lands due to symmetry. As depicted in Fig. 1, the film thickness, denoted as h, can be defined as follows [13]:

$$h = h_0 \left(1 - \varepsilon\right). \tag{1}$$

where h_0 is the initial film thickness; $\varepsilon(y/h_0)$ is the eccentricity ratio; y is the damper displacement and e is the recess depth.

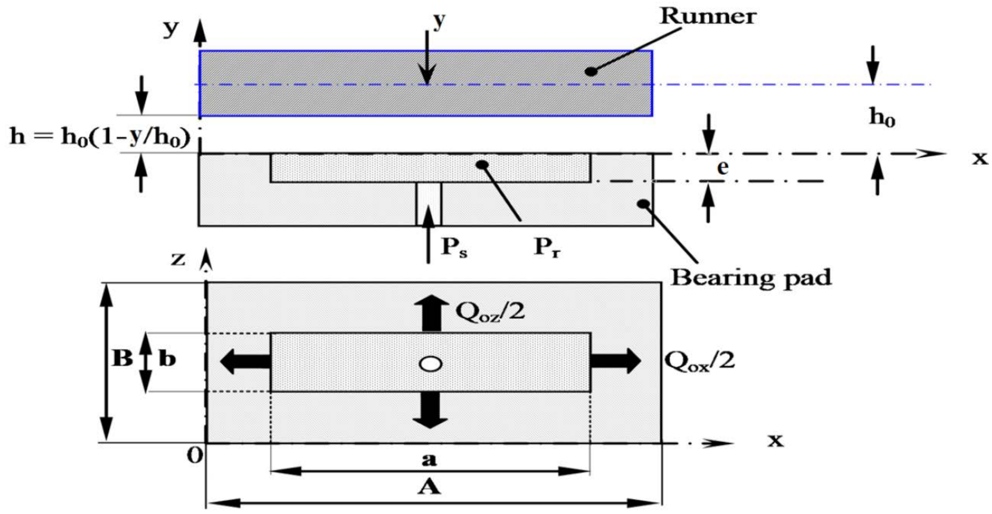

Fig. 1. Rectangular hydrostatic bearing flat pad.

The recess pressure, for each hydrostatic bearing pads (Fig. 1), is determined by solving of the following flow continuity equation for pure hydrostatic (no moving surface, $dh/dt = 0$):

$$Q_r = Q_{ox} + Q_{oz}\,, \tag{2}$$

where

$$Q_r = \frac{\pi c_d\, d_o^2}{\sqrt{8\rho}}\sqrt{(P_s - P_r)}, \tag{3}$$

$$Q_{ox} = 2\int_0^{B/2}\int_0^h u_x dz dy\,; \quad Q_{oz} = 2\int_0^{A/2}\int_0^h u_z dx dy\,, \tag{4}$$

$$u_x = \frac{1}{2\mu}\frac{\partial P}{\partial x}(y-h)\,y\,; \quad u_z = \frac{1}{2\mu}\frac{\partial P}{\partial z}(y-h)\,y \tag{5}$$

where d_o is the orifice diameter; ρ is the density; Q_{ox} and Q_{oz} are the oil flow of the hydrostatic bearing pad in the x, and z directions, respectively, Q_r represents the flow through a orifice restrictor; u_x, u_y and u_z are the flow velocities in the x, y and z directions, respectively; P_s is a supply pressure and P_r is the recess pressure, c_d is the orifice discharge coefficient. Note that the discharge coefficient C_d is a function of the Reynolds number, Re. Typically it varies in a nonlinear fashion from $C_d \approx 0.3$ for Re ≈ 2 to $C_d \approx 0.7$ at Re ≈ 100, and drops to about $C_d \approx 0.6$ for higher Re values [14].

It must be noticed that when the orifice length l is no longer negligible, the discharge coefficient C_d, can be determined by means of the following equations [14].

$$C_d = \left[1.5 + 13.74\left(\frac{l}{d_0\mathrm{Re}}\right)^{1/2}\right]^{-1/2} \quad \text{for} \quad \frac{d_0\mathrm{Re}}{l} > 50\,, \tag{6}$$

$$C_d = \left[2.5 + 64\left(\frac{l}{d_0\mathrm{Re}}\right)\right]^{-1/2} \quad \text{for} \quad \frac{d_0\mathrm{Re}}{l} < 50\,. \tag{7}$$

The feeding Reynolds number for an orifice is as follows [14]:

$$\mathrm{Re} = \frac{d_o}{\mu}\left[2\rho\left(P_s - P_r\right)\right]^{1/2} \tag{8}$$

4 Numerical Modelling

4.1 Reynolds equation approach

The Reynolds equation facilitates the calculation of the pressure distribution $P(x, z, t)$. In the case of an incompressible, laminar, isoviscous, and inertialess fluid, the Reynolds equation can be expressed as [3]:

$$\frac{\partial}{\partial x}\left(h^3\frac{\partial P)}{\partial x}\right) + \frac{\partial}{\partial z}\left(h^3\frac{\partial P)}{\partial z}\right) = 12\,\mu V\,, \tag{9}$$

where $0 \leq x \leq A$ and $0 \leq z \leq B$; P is the hydrostatic pressure field of the hydrostatic bearing pad; h is the film thickness of the hydrostatic bearing pad; V is the squeeze velocity of the hydrostatic bearing pad; μ is the dynamic viscosity.

4.2 Computational fluid dynamics

In the current model, cavitation is disregarded as the minimum pressure does not fall below the vapor pressure. The conservation equation applies to steady-state flow that is incompressible, isoviscous, isothermal, and devoid of gravitational effects.The governing equations are as follows:

Continuity equations:

$$\frac{\partial u_i}{\partial x_i} = 0\,. \tag{10}$$

Momentum equation:

$$\rho\frac{\partial(u_i u_j)}{\partial x_i} = -\frac{\partial P}{\partial x_i} + \frac{\partial}{\partial x_i}\left[\mu\left(\frac{\partial u_j}{\partial x_i} + \frac{\partial u_i}{\partial x_j} - \frac{2}{3}\delta_{ij}\frac{\partial u_k}{\partial x_k}\right) - \partial\overline{\rho u'_i u'_j}\right]\,, \tag{11}$$

where $U = (u_i, u_j, u_k)$ is the velocity vector, P is the static pressure, μ is the dynamic viscosity, ρ is the density.

The three-dimensional full Reynolds Averaged Navier Stokes (RANS) equations, encompassing both momentum and continuity equations, are employed to determine the pressure distribution within the hydrostatic bearing. The computational fluid dynamics software utilized for this simulation is ANSYS-CFX-19.2.

MESH TYPE AND SOLUTION PROCEDURE

In this research, the three-dimensional steady incompressible Reynolds-Averaged Navier-Stokes (RANS) equations were resolved using ANSYS CFX. The equations were closed with the Shear Stress Transport (SST) k-ω turbulence model, which functions by employing a turbulence/frequency-based model (k-ω) in proximity to the wall and a k-ε model in the bulk flow region. To ensure accurate predictions of near-wall flow behavior, the first grid points are positioned at $y+$ values less than 1, as recommended by this model. Conversely, the k-ε model is utilized in fully turbulent conditions. This approach provides highly precise predictions regarding the initiation and extent of flow separation under adverse pressure gradients [15]. Finer mesh configurations are implemented in the transition zone between the recess and the fully developed film thickness to illustrate the influence of the feeding Reynolds number on static pressure, recess pressure, Rayleigh step effect, and inertia effect.

As illustrated in Fig. 2, the computational domain encompasses several surfaces: the orifice feed-line, the recess, the sill, and the film thickness. It is important to

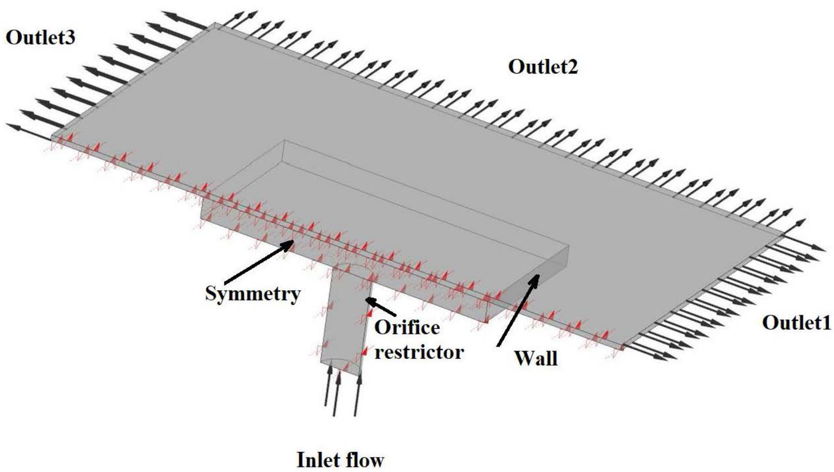

Fig. 2. Computational domain and boundary conditions.

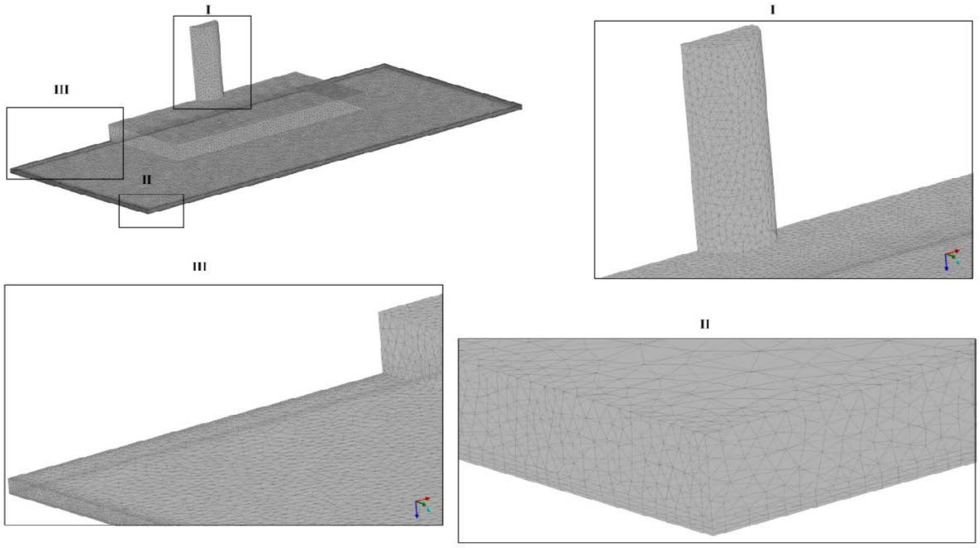

Fig. 3. Computational domain for recess depth, $e/h_0 = 4$ (Number of grid elements is 600409).

note that all geometric parameters and boundary conditions have been accurately replicated in accordance with the numerical analysis based on the Reynolds equation methods discussed in Section 3.1 (Reynolds boundary conditions). Adiabatic and no-slip conditions are applied to the wall. The wall boundary condition incorporates the orifice restrictor. At the orifice entrance, a constant static pressure supply is maintained, and a laminar flow regime is enforced. The outlets are defined with a reference pressure set to absolute zero (Pascal). Given the geometric axial symmetry and the uniform boundary conditions at the axial extremities of the model, only one half of the axial geometry is analyzed. This application of symmetry boundary conditions effectively reduces both the grid size and the computational time.Convergence is achieved when the root-mean-squared (RMS) residual values for all flow parameters (u, v, w, and p) fall below 10^{-5}.

The computational domain is divided into tetrahedral elements for two recess depths: (a) $e/h = 4$ and (b) $e/h = 152$. Figure 3 illustrates the grid for $e/h = 4$, featuring an enlarged view of the injection area and the recess extremity. The geometry was grided using the ICEM-CFD mesh generator that is part of the ANSYS-CFX software.

5 Numerical Results

5.1 Effect of the feeding Reynolds number and static eccentricity ratios predicted from Reynolds equation

This section examines the variations in supply pressure, recess pressure, and pressure ratio as they relate to the feeding Reynolds number across different static eccentricity ratios. The bearing characteristics are defined as follows: bearing pad length A is 0.037 m; bearing pad width B is 0.037 m; the dimension ratio $a/A = b/B$ is 0.5; restrictor diameter d_o is 2.49 mm, the height of orifice restrictor is 6 mm and the recess depth is $e/h = 152$. Figures 4a and 4b illustrate the impact of the feeding Reynolds number and static eccentricity on the supply and recess pressures of a hydrostatic bearing flat pad. These findings were derived using the Reynolds equation. The effects of the static eccentricity ratio and feeding Reynolds number, calculated from the supply pressure at a viscosity of 0.05 Pa.s, are depicted in Fig. 4a.

the findings indicate that the feeding Reynolds number rises in response to an increase in supply pressure. It is important to note that when the feeding Reynolds number is held constant, the supply pressure escalates with an increase in static eccentricity. Furthermore, when the supply pressure remains constant, the feeding Reynolds number is observed to increase as the static eccentricity ratio decreases, attributed to the growth in film thickness. Figure 4b illustrates the relationship between the feeding Reynolds number and static eccentricity ratio on recess pressure at a viscosity of 0.05 Pa.s. This graph demonstrates that as the static eccentricity ratio

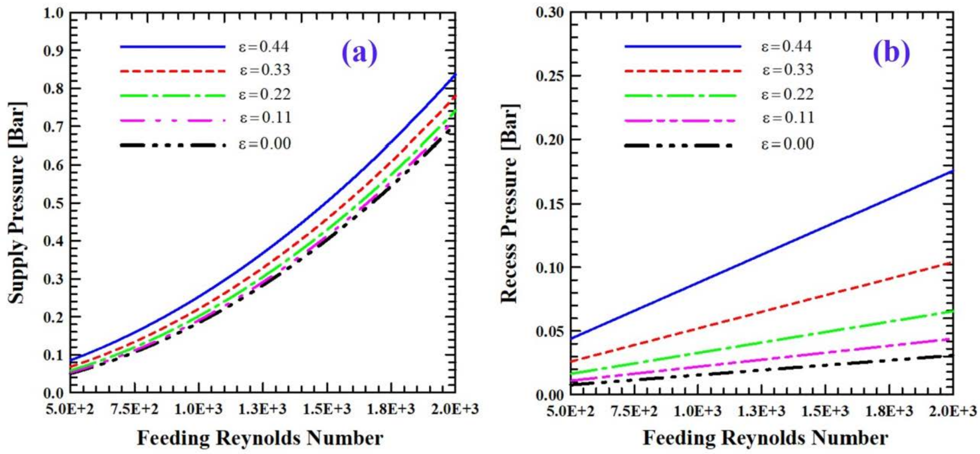

Fig. 4. Supply pressure (a), recess pressure (b), versus feeding Reynolds number at different static eccentricity ratio predicted from Reynolds equation.

increases from 0.0 to 0.44, the recess pressure also rises due to a reduction in film thickness. The data reveal a linear relationship between recess pressure and feeding Reynolds number. It is noteworthy that when the static eccentricity exceeds 0.33, there is a marked increase in recess pressure, which correlates with the rise in supply pressure (refer to Fig. 4a). The recess pressure is calculated by solving the flow continuity equation for varying film thicknesses.

5.2 Comparison between Reynolds equation and CFD- CFD-ANSYS-CFX

To validate the numerical analysis conducted using Computational Fluid Dynamics (CFD), a comparison was made as illustrated in Fig. 5, contrasting the results from the Reynolds approach with those from the CFD simulation. This analysis specifically targeted a low Reynolds number model, which is confined to laminar flow conditions within the recess of a hydrostatic bearing. The results demonstrate a significant correlation between the CFD outcomes and those obtained through the Reynolds equation methods, particularly when the Reynolds number in the recess is less than 1000.

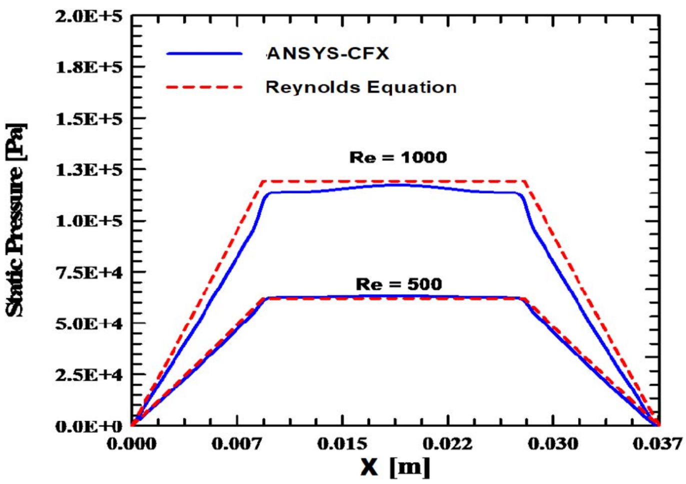

Fig. 5. Comparison of Reynolds equation and CFD- CFD-ANSYS-CFX: $e/h_0 = 152$, static pressure for Re $= 500$ and Re $= 1000$.

5.3 Effect of the feeding Reynolds number, recess depth and viscosity on static pressure

Figure 6(a,b) illustrates the impact of the feeding Reynolds number and viscosity on the static pressure as predicted by ANSYS-CFX. The film thickness is maintained at

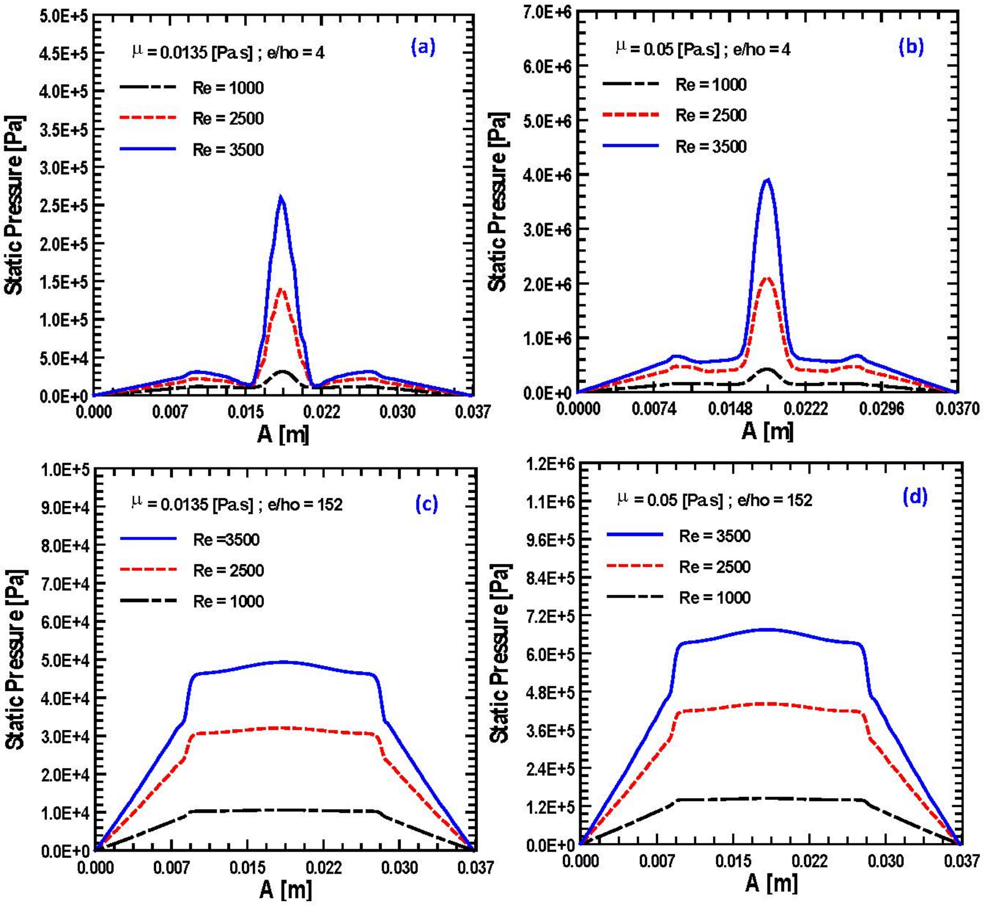

Fig. 6. Effect of the feeding Reynolds number on static pressure predicted from ANSYS-CFX: (a) $\mu = 0.0135$ Pa.s and $e/h_0 = 4$; (b) $\mu = 0.05$ Pa.s and $e/h_0 = 4$; (c) $\mu = 0.0135$ Pa.s and $e/h_0 = 152$; (d) $\mu = 0.0135$ Pa.s and $e/h_0 = 152$.

0.337 mm (with a static eccentricity ratio of 0.44). Figures 6a and 6b depict the effect of the feeding Reynolds number on static pressure for two distinct viscosities: (a) $\mu = 0.0135$ Pa.s and (b) $\mu = 0.005$ Pa.s. The recess depth, e/h_0, is held constant at 4. These findings indicate that the static pressure within the recess area is not uniform. It is important to note that increasing the feeding Reynolds number from 1000 to 3500 leads to more pronounced pressure peaks near the restrictor area, attributed to the elevated supply pressure, as the pressure peaks rise in response to the increase in supply pressure (refer to Fig. 1).

Conversely, a reduction in pressure is noted between the restrictor region (injection zone) and the recess's terminus, attributed to the Rayleigh step effect, which leads to the formation of a significant Main Vortical Cell (MVC). This observation is corroborated by the findings of Horvat and Frêne [11, 15]. Figures 6c and 6d illustrate the influence of the feeding Reynolds number and viscosity on static pressure for two distinct viscosities: (a) $= 0.0135$ Pa.s and (b) $= 0.05$ Pa.s, while maintaining a constant recess depth of 152 (e/h_0). The data indicates that the pressure distribution within the recess stabilizes, with the jet flow becoming fully diffused. Notably, there are no pronounced pressure peaks surrounding the restrictor area, nor is there a Rayleigh step effect when the recess depth is fixed at 152. Additionally, Figs. 6c and 6d reveal that an increase in the feeding Reynolds number, resulting from a rise in supply pressure from 1000 to 3500, leads to a progressive increase in pressure within the housing. This phenomenon can be attributed to the inertia effect caused by a sudden change in geometry between the orifice outlet and the housing configuration. It is also important to highlight that both static pressure and housing pressure rise with increasing viscosity.

5.4 Effect of the eccentricity ratio on static pressure

Figures 7a and 7b illustrate the influence of the eccentricity ratio on the static pressure as predicted by CFD-ANSYS-CFX, specifically for a low viscosity of 0.0135 Pa.s and two distinct feeding numbers: (a) Re $= 1000$ and (b) Re $= 3500$, while maintaining a constant recess depth of 152. These illustrations reveal that an increase in the

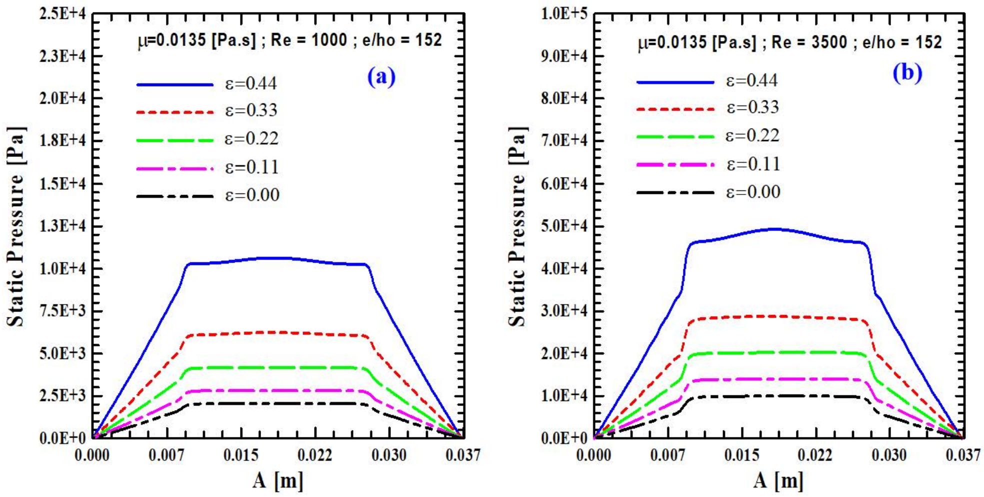

Fig. 7. Effect of the film thickness on static pressure at recess depth of 152 predicted from ANSYS-CFX: (a) $\mu = 0.0135$ Pa.s and Re $= 1000$; (b) $\mu = 0.0135$ Pa.s and Re $= 3500$.

eccentricity ratio corresponds to a rise in static pressure, attributed to the elevated supply and recess pressures, as depicted in Figures 4a and 4b. Additionally, Figs. 7a and 7b further indicate that the static pressure increases with the eccentricity ratio, which ranges from 0 to 0.44, primarily due to the corresponding increase in supply pressure.

6 Conclusion

In the current study, a three-dimensional computational fluid dynamics (CFD) model has been established utilizing ANSYS-CFX to investigate the impact of flow regimes in recess on the pressure distribution within a hydrostatic bearing flat pad supplied by an orifice restrictor. The pressure distribution and comprehensive flow characteristics of the bearing are determined by solving the full 3D Navier-Stokes equations in conjunction with the SST k-ω turbulence model using ANSYS-CFX 19.2. A comparison of the outcomes from the developed 3D CFD model with those derived from the Reynolds equation, which is limited to laminar flow conditions, revealed a high degree of correlation between the two approaches. Following validation, the model was employed to examine the influence of various parameters, including the feeding Reynolds number, recess depths, viscosity, and static eccentric ratio, on the pressure profile. The findings from the numerical simulations can be succinctly summarized as follows:

- The pressure exerted by the supply related to the feeding Reynolds number has led to an increase in the pressure ratio within the recess. Additionally, as the film thickness gradually increases with the eccentricity ratio, the static pressure attains higher values. In the case of a shallow recess ($e/h0 = 4$), the static pressure distribution within the recess area is not uniform. It is important to note that an increase in the feeding Reynolds number, in conjunction with the corresponding pressure supply, results in more pronounced pressure peaks near the restrictor area, attributed to the elevated supply pressure. Furthermore, a pressure drop is observed between the restrictor area (injection zone) and the recess's end, which is caused by the Rayleigh step effect, leading to the formation of a significantly developed Main Vortical Cell. These findings have been corroborated by the research conducted by Horvat and Frêne [11, 15].

- At extremely low viscosity of 0.0135 Pa.s and in deeper recesses $e/h_0 = 152$, the pressure drop reaches a ratio of 0.5 relative to atmospheric pressure, leading to a non-operational state where the efficiency of the lubrication process diminishes. In the case of deep recesses ($e/h_0 = 152$), the pressure distribution within the recess tends to stabilize, with the jet flow becoming fully diffused. It is important to highlight that there are no significant pressure peaks near the restrictor area, nor is there a Rayleigh step effect observed. Additionally, an increase in the feeding Reynolds number correlates with a rise in the pressure ratio and the inertial effects. Furthermore, both static pressure and recess pressure are observed to increase with higher viscosity levels. Moreover, an increase in the eccentricity ratio also leads to an enhancement in the pressure ratio and the inertial effects.

REFERENCES

[1] CAI-WAN CHANG-JIAN, HER-TERNG YAU, JIANN-LIN CHEN (2010) Nonlinear dynamic analysis of a hybrid squeeze-film damper-mounted rigid rotor lubricated with couple stress fluid and active control. *Applied Mathematical Modelling* **34**(9) 2493-2507.

[2] A. BOUZIDANE, M. THOMAS (2013) Nonlinear Dynamic Behavior of a Flexible Shaft Supported by Smart Hydrostatic Squeeze Film Dampers. *Journal of Tribology* **135**(3) 31701.

[3] A. BOUZIDANE, M. THOMAS (2007) Equivalent Stiffness and Damping Investigation of a Hydrostatic Journal Bearing. *Tribology Transactions* **50**(2) 257-267.

[4] A. BOUZIDANE, M. THOMAS (2013) Nonlinear Dynamic Analysis of a Rigid Rotor Supported by a Three-Pad Hydrostatic Squeeze Film Dampers. *Tribology Transactions* **56**(5) 717-727.

[5] L.A. SAN ANDRES, J.F.M. VELTHUIS (1992) Laminar Flow in a Recess of a Hydrostatic Bearing. *Tribology Transactions* **35**(4) 738-744.

[6] M.J. BRAUN, F.K. CHOY, Y.M. ZHOU (1993) The Effects of a Hydrostatic Pocket Aspect Ratio, Supply Orifice Position, and Attack Angle on Steady-State Flow Patterns, Pressure, and Shear Characteristics. *Journal of Tribology* **115**(4) 678-85.

[7] M.J. BRAUN, M. DZODZO (1995) Effects of Hydrostatic Pocket Shape on the Flow Pattern and Pressure Distribution. *International Journal of Rotating Machinery* **1**(3-4) 745046.

[8] M.J. BRAUN, M. DZODZO (1995) Effects of the Feedline and the Hydrostatic Pocket Depth on the Flow Pattern and Pressure Distribution. *Journal of Tribology* **117**(2) 224-32.

[9] M. HELENE, M. ARGHIR, J. FRÊNE (2003) Numerical Study of the Pressure Pattern in a Two-Dimensional Hybrid Journal Bearing Recess, Laminar, and Turbulent Flow Results. *Journal of Tribology* **125**(2) 283-90.

[10] M.J. BRAUN, M.B. DZODZO (1997) Three-Dimensional Flow and Pressure Patterns in a Hydrostatic Journal Bearing Pocket. *Journal of Tribology* **119**(4) 711-19.

[11] F.E. HORVAT, M.J. BRAUN (2011) Comparative Experimental and Numerical Analysis of Flow and Pressure Fields Inside Deep and Shallow Pockets for a Hydrostatic Bearing. *Tribology Transactions* **54**(4) 548-567.

[12] S.I. MOLDOVAN, M.J. BRAUN, A.M. BALASOIU (2013) A Three-Dimensional Parametric Study and Numerical/Experimental Flow Visualization of a Six-Pocket Hydrostatic Journal Bearing. *Tribology Transactions* **56**(1) 1-26.

[13] S.R. SCHMID, B.J. HAMROCK, B.O. JACOBSON (2013) "Fundamentals of Machine Elements". CRC Press.

[14] J. BARDINA, P. HUANG, T. COAKLEY (1997) Turbulence modeling validation. In: *28th Fluid Dynamics Conference* 29 June 1997 - 02 July 1997, Snowmass Village, CO, U.S.A.

[15] J. FRÊNE, M. ARGHIR, V. CONSTANTINESCU (2006) Combined thin-film and Navier–Stokes analysis in high Reynolds number lubrication. *Tribology International* **39**(8) 734-747.